Secondary Instabilities of Hexagonal Patterns in a Bénard-Marangoni Convection Experiment

Denis Semwogerere and Michael F. Schatz

Center for Nonlinear Science and School of Physics, Georgia Institute of Technology, Atlanta, Georgia 30332-0430, USA

(Received 5 September 2003; published 17 September 2004)

We have identified experimentally secondary instability mechanisms that restrict the stable band of wave numbers for ideal hexagons in Bénard-Marangoni convection. We use "thermal laser writing" to impose long wave perturbations of ideal hexagonal patterns as initial conditions and measure the growth rates of the perturbations. For $\epsilon = 0.46$ our results suggest a longitudinal phase instability limits stable hexagons at a high wave number while a transverse phase instability limits low wave number hexagons.

DOI: 10.1103/PhysRevLett.93.124502 PACS numbers: 47.54.+r, 47.20.–k, 61.72.Ji

For stable, spatially periodic patterns observed in many nonequilibrium systems [1–4], the pattern typically exhibits a wave number q that is drawn from a range of possible values, even when a given system's external parameters are fixed. The maximum and minimum values of q are typically limited by a secondary instability that leads to more complex states. For stationary striped patterns (rolls), the study of secondary instability in Rayleigh-Bénard convection led to the identification of several instability mechanisms, as cataloged by the "Busse Balloon" [5]. These mechanisms have a universal character and have been associated with roll instability in several other physical systems [6–8]. Periodic patterns of hexagons also arise in diverse physical settings, including fluid flow [9,10], chemical reactions [11], nonlinear optics [12], crystal growth [13], and granular flow [14]. However, the instability mechanisms that constrain stable wave numbers for hexagons have not, heretofore, been observed in experiments.

In this Letter we describe phase instabilities that limit the stable wave number of hexagonal patterns in Bénard-Marangoni convection experiments. These instabilities initially appear as modulations with small wave number k of the hexagons. Theoretical studies of amplitude equations show that as $k \to 0$ two different instabilities can restrict the stable band [15,16]—a *longitudinal* modulation with a curl-free phase vector $\mathbf{\Phi}$ and a *transverse* modulation with a divergence-free $\mathbf{\Phi}$. Our experiments demonstrate that these instabilities are observable even with finite k where significant mixing of the longitudinal and transverse modes might occur [16].

In Bénard-Marangoni convection hexagonal convection patterns arise when a fluid with a free upper surface is heated uniformly from below and cooled from above with a sufficiently large temperature gradient. The convective flow is driven primarily by temperature-induced surface tension gradients (*thermocapillarity*) at the liquid-gas interface and is characterized by the Marangoni number $M = \sigma_T \Delta T d/\rho\nu\kappa$, where σ is the liquid's surface tension, ΔT the temperature difference across the liquid layer, $\sigma_T \equiv d\sigma/dT$, and d, ρ, ν, κ are, respectively, the liquid's thickness, density, kinematic viscosity, and thermal conductivity. With $\sigma_T < 0$, surface tension gradients draw fluid from warm areas at the liquid-gas interface to cool areas. This creates upflows at the locally warm spots and downflows at the cool areas [Fig. 1(a)].

The experiments are performed on a flat layer of silicone oil of depth $d = 0.094 \pm 0.003$ cm confined by a Teflon sidewall ring of inner diameter 7.62 ± 0.003 cm

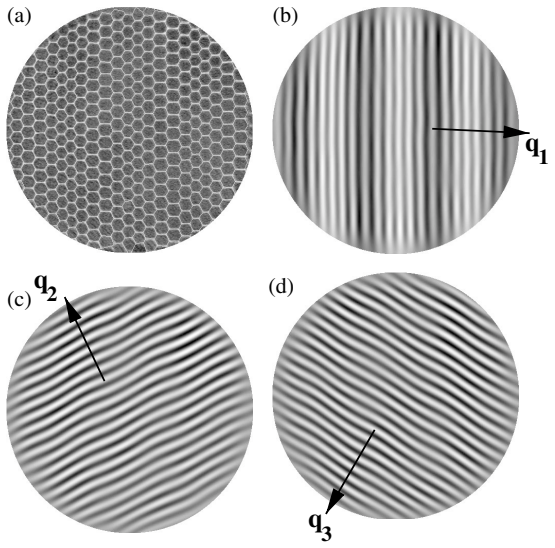

FIG. 1. Shadowgraph image (a) of hexagons with a longitudinal phase perturbation is shown with the pattern's three roll components (b)–(d) extracted by complex demodulation. For the purposes of illustration, the perturbation, imposed as an initial condition, is shown with an amplitude that is larger than typical modulations by a factor of 8. In (a), the white edges and dark centers of the hexagons indicate, respectively, regions of downflow and upflow. (b) The main modulation is to the $\mathbf{q}_1$ rolls—note their compression and dilation. Shading has been added to emphasize the long wave nature of the modulation—the overall lighter areas have higher wave number than the darker regions. (c) $\mathbf{q}_2$ rolls are sheared slightly by the modulation. (d) The $\mathbf{q}_3$ rolls are modulated with the same amplitude and phase as the $\mathbf{q}_2$ rolls.

 0031-9007/04/93(12)/124502(4)$22.50

yielding an aspect ratio of 40.5 for the convecting region. Uniform heating is applied from below and an air gap of thickness 0.074 ± 003 cm is cooled from above to set the control parameter at $\epsilon = [(M - M_c)/M_c] = 0.46$, where M_c is the value of the Marangoni number at the onset of convection. The liquid kinematic viscosity ν is 8.25 ± 0.03 cS and Prandtl number Pr is 87.2 ± 0.3. All measurements are nondimensionalized by the length scale d and the vertical diffusion time $\tau_v = d^2/\kappa = 8.8$ s. Visualization is achieved using the shadowgraph technique (see Fig 1) [17]. Images of the patterns are digitized and then analyzed using a variety of Fourier and complex demodulation techniques to extract the spatial dependence of the pattern wave number, amplitude and phase [18–20]. A hexagonal pattern can be decomposed into three component roll patterns oriented 120° with respect to one another. The components are labeled as in Fig. 1 by wave vectors $\mathbf{q}_1$, $\mathbf{q}_2$, and $\mathbf{q}_3$.

The initial conditions of the experiment are imposed by thermo-optically altering the thermocapillary driving [21]. Beginning at fixed ϵ above onset the natural pattern selected by the system is replaced with the desired pattern by heating multiple spatial points along the liquid-gas interface with a scanned infrared CO_2 laser beam. The imposed hot spots become the new regions of liquid upflow thereby establishing the pattern [Fig. 1(a)] The process typically takes less than 10 τ_v, whereupon lasing is turned off. The strong thermal gradients due to the lasing dissipate within $\sim\tau_v$ and thereafter the resulting pattern sets the initial condition from which the subsequent pattern evolution is studied. Lasing is maintained along the outer 25% of the pattern to pin cells in a hexagonal boundary so as to prevent pattern distortion due to creation or destruction of cells at the sidewall.

Imposing ideal hexagons (i.e., patterns with $q = |\mathbf{q}_1| = |\mathbf{q}_2| = |\mathbf{q}_3|$) permits measurement of the stable band but is insufficient to determine the mechanisms of the secondary instabilities. The band is determined by imposing ideal patterns at fixed ϵ, and tracking q over time to check for stability [21]. The imposed pattern remains stationary for q in a stable range; however, if q is too large or too small, the imposed pattern becomes unstable. The boundary is taken to be the largest and smallest q that do not change. For unstable values of q the pattern forms penta-hepta defects at the boundaries or within the interior. The defects propagate in such a way as to either add or eliminate cells so that the average q is driven into the stable band [21]. Observation of these instability driven dynamics does not reveal the nature of the mechanisms that cause them, unlike the case of periodic rolls where phase instabilities such as the zigzag instability are easily distinguished by eye [5].

The mechanisms of secondary phase instability can be probed by applying phase perturbations to hexagonal patterns (Figs. 1 and 2). The perturbations are characterized by a wave vector $\mathbf{k}$ and angle θ measured with respect to one of the roll wave vectors (with $\mathbf{q}_1$ chosen here for convenience). In the long wavelength limit

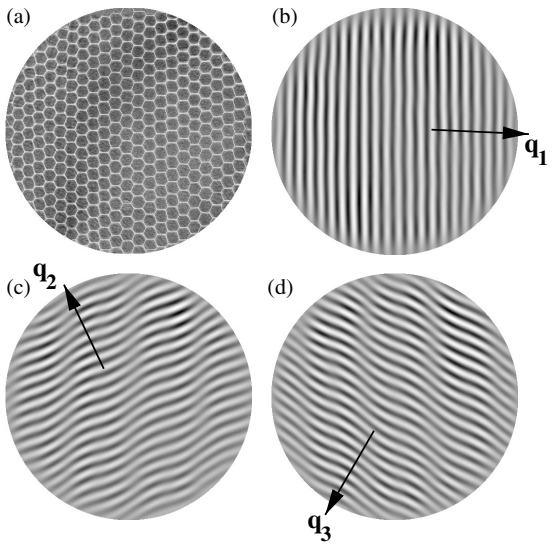

FIG. 2. Shadowgraph image (a) of hexagons with a transverse phase perturbation is shown with the pattern's three roll components (b)–(d) extracted by complex demodulation. For the purposes of illustration, the perturbation is shown with an amplitude that is larger than typical modulations by a factor of 9. (b) The $\mathbf{q}_1$ component is unaffected by the transverse modulation. (c) The roll component labeled by wave vector $\mathbf{q}_2$ that shows the shearing of the rolls in a direction transverse to the $\mathbf{q}_1$ rolls. (d) The $\mathbf{q}_3$ component is modulated with the same amplitude but opposite phase as the $\mathbf{q}_2$ component.

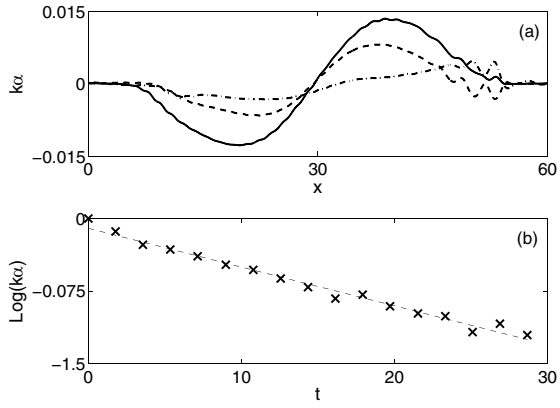

FIG. 3. Spatial and temporal evolution of the longitudinal phase perturbation. (a) The profile of the local wave number of the $\mathbf{q}_1$ rolls (scaled by the mean value $q = 2.08$) is plotted at times $t = 0$ (solid line), $t = 13$ (dashed line) and $t = 27$ (dot-dashed line); thus the phase modulation adjusts the overall wave number by a maximum of less than 1.5%. The long wave nature of the perturbation is apparent—the modulation wave number $k = 0.14$ is approximately 1/15th of the mean q. (b) The amplitude ($k\alpha$) is plotted as a function of time on a semilog scale; the slope of this curve yields the growth rate, which is negative for perturbations within the stable band.

($k \to 0$) the phase vector of the perturbation can be written as $\mathbf{\Phi} \equiv -(\phi_2 + \phi_3)\hat{\imath} + (\phi_2 - \phi_3)/\sqrt{3}\hat{\jmath}$ [15,16], where ϕ_1, ϕ_2, and ϕ_3 are terms added to the phases of the $\mathbf{q}_1$, $\mathbf{q}_2$, and $\mathbf{q}_3$ rolls, respectively. In that case there are two classes of phase perturbation: a longitudinal perturbation for which $\mathbf{\Phi} \| \mathbf{k}$ and a transverse perturbation for which $\mathbf{\Phi} \perp \mathbf{k}$. For $\theta = 0$ the longitudinal perturbation is taken as $\phi_1 = i\alpha \cos kx$, $\phi_2 = -i\frac{1}{2}\alpha \cos kx$, and $\phi_3 = -i\frac{1}{2}\alpha \cos kx$ (Fig. 1), where the x axis is parallel to $\mathbf{q}_1$. The result is a sinusoidal modulation of the wave number of the $\mathbf{q}_1$ rolls in a direction parallel to $\mathbf{k}$ with amplitude $k\alpha$ [Fig. 3(a)]. The perturbations to the $\mathbf{q}_2$ and $\mathbf{q}_3$ rolls have similar modulations parallel to $\mathbf{k}$ but with amplitude $\frac{1}{2}k\alpha$. For the transverse perturbation $\phi_1 = 0$, $\phi_2 = i(\sqrt{3}/2)\alpha \times \cos kx$ and $\phi_3 = -i\alpha(\sqrt{3}/2)\cos kx$. In that case the $\mathbf{q}_1$ rolls are unperturbed while the $\mathbf{q}_2$, and $\mathbf{q}_3$ rolls are perturbed sinusoidally along the x axis with amplitude $(\sqrt{3}/2)k\alpha$.

Perturbations applied at fixed ϵ decay exponentially when q is within the stable band and do so with a growth rate that depends on q. The growth rate is measured by first applying the perturbation as an initial condition and then tracking the evolution of its amplitude. The logarithm of the amplitude plotted against time fits reasonably well to a straight line [Fig. 3(b)] indicating that the perturbations decay exponentially as expected for disturbances that are sufficiently small. The slope obtained from a linear least squares fit yields the perturbation's growth rate.

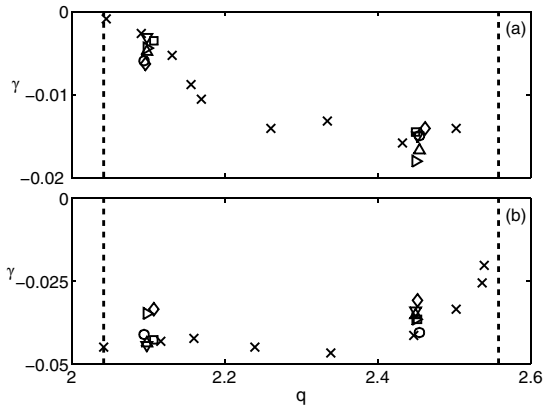

FIG. 4. Plots of growth rate vs wave number for the transverse perturbation (a) and the longitudinal perturbation (b) at fixed modulation wave number $k = 0.14$. The dashed lines represent experimentally measured boundaries of the stable band measured previously for $\epsilon = 0.46$. At that value of ϵ the boundaries are in the $0 < \epsilon < 0.5$ range where they were found to approximately coincide with theoretical predictions by Bestehorn for Bénard-Marangoni convection [10,21]. (a) The growth rate for the transverse perturbation appears to go to zero at the low wave number boundary. (b) The growth rate of the longitudinal perturbation appears to sharply decrease and trend to zero at the high wave number boundary. The data are shown for $\theta = 0$ ($\times$,$\bigcirc$), $\theta = \pi/18$ ($\square$), $\theta = \pi/12$ ($\diamond$), $\theta = \pi/6$ ($\triangleright$), $\theta = \pi/3$ ($\triangle$), and $\theta = 2\pi/3$ ($\triangledown$).

Secondary instabilities are identified by observing the behavior of their growth rates at the boundaries of the stable band. The growth rate of the transverse perturbation is found to remain relatively constant for $2.2 \lesssim q \lesssim 2.55$ but starts to gradually decrease in magnitude for $q \lesssim 2.2$ until it crosses zero at the low wave number boundary [Fig. 4(a)]. This suggests that the divergence-free transverse perturbation becomes unstable at the low wave number side of the stable band and is thus responsible for the instability at that boundary. At the high wave number boundary the magnitude of the growth rate does not reduce, i.e., the transverse modulation does not appear to restrict the band at high wave number. For the longitudinal phase perturbation the measured growth rate is finite at the low wave number boundary and remains constant for $2.05 \lesssim q \lesssim 2.4$. As q approaches the high wave number boundary the change in growth rate is not slow as in the transverse case, but becomes increasingly sharp the closer q gets to the boundary, and appears to trend to zero growth rate at the boundary [Fig. 4(b)], i.e., the longitudinal perturbation may be the secondary instability that restricts the stable band at high wave number.

Amplitude equation analyses [16,22] suggest that phase perturbations with finite k are neither purely transverse nor purely longitudinal, i.e., for longitudinal perturbations $\mathbf{k}$ is not parallel to $\mathbf{\Phi}$ and for transverse perturbations $\mathbf{k}$ is not perpendicular to $\mathbf{\Phi}$. This "mixing" of phase perturbations is a function of θ and is in general nonzero except for $\theta = n\pi/6$, where n is an integer. A consequence of this is that the growth rates of phase perturbations are also functions of θ. In the experiments, with $k = 0.14$ and at two different values of q in the stable band, growth rates were measured for $\theta = n\pi/6$, for $n = 1$, 2, and 4. The results were not significantly different (Fig. 4) indicating no mixing, consistent with theory [16]. For $\theta = \pi/12$ and $\pi/18$ where mixing is expected to be strong, the growth rates were also not significantly different, suggesting that k is small enough that phase mixing is weak.

For a given q within the stable band, perturbations become more strongly damped as k is increased. However, the trend of the growth rate toward zero at the low wave number boundary for transverse perturbations, and at the high wave number boundary for longitudinal perturbations appears unchanged (Fig. 5). The growth rates of perturbations with $k < 0.14$ are small and could not be measured reliably; however, the trend of the data suggests that *decreasing* k results in *weaker* damping, i.e., the least stable perturbations are of long wavelength.

Mechanisms other than phase instabilities might also play a role in limiting the stable wave number band. The growth rate data conclusively show that the transverse perturbation becomes unstable at the low q boundary. The

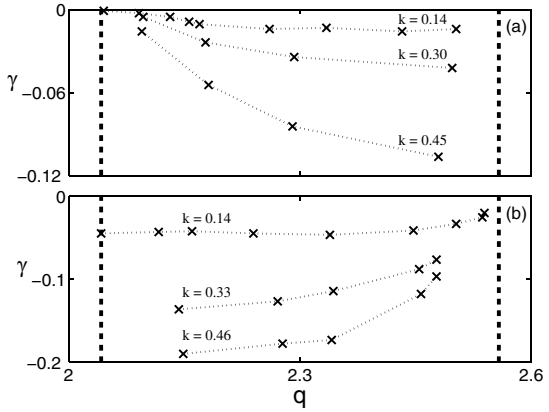

FIG. 5. Plots of growth rate vs wave number with varied modulation wave number k for the transverse perturbation (a) and the longitudinal perturbation (b). (a) The growth rate of the transverse perturbation appears to go to zero at the low wave number boundary for all k. (b) Like the case of $k = 0.14$ the growth rate of the longitudinal perturbation appears to decrease and trend to zero at the high wave number boundary for $k = 0.30$ and $k = 0.45$. Data points for q close to the boundaries could not be obtained for large k because the modulations are strong enough to create regions where the local wave number falls outside the stable band, leading to pattern breakdown.

data are less convincing at the high q boundary where the growth rates of the longitudinal perturbation are trending toward zero so rapidly the resolution of our current experiments is insufficient to resolve very small growth rates near the boundary. In principle, amplitude instabilities could limit the stable band at high q; however, theoretical work on the Bénard-Marangoni convection [10] suggests that when buoyancy effects are weak, amplitude instabilities play no role in secondary instability of hexagons.

Some insight into the ϵ dependence of secondary instability mechanisms can be gained by comparing these results with previous measurements of the stable wave number band [21]. The measured low q boundary does not change significantly for $0 < \epsilon < 1$ suggesting that the transverse phase instability is the mechanism that limits the stable band for that range. Similarly, the high q boundary remains unchanged for $0.4 \lesssim \epsilon < 1$, suggesting the longitudinal phase instability governs the high q limit. However, for $\epsilon \lesssim 0.4$ the high q limit depends strongly on ϵ. Thus, by analogy with the Busse balloon for straight rolls, where a change in the nature of the ϵ dependence of the stability boundaries *can* indicate transitions between different mechanisms, it is possible that the dominant instability mechanism may change (say from a longitudinal to a transverse phase instability) as ϵ is decreased below 0.4. Future experimental work complemented by theoretical and numerical studies at the same parameter values would be useful to map the dependence of secondary instability mechanisms on ϵ and elucidate the relative importance of phase and amplitude instabilities.

We thank Yuan-Nan Young and Hermann Riecke for reading an early version of this Letter and for many helpful discussions. We also thank Keng-Hwee Chiam and Mark Paul for the use of their local wave number analysis code. Support for this work by the National Science Foundation and the Research Corporation is gratefully acknowledged.

[1] L. Rayleigh, Philos. Mag. **32**, 529 (1916).
[2] A. M. Turing, Philos. Trans. R. Soc. London B **237**, 37 (1952).
[3] E. Dubois-Violette, G. Durand, E. Guyon, P. Manneville, and P. Pieranski, in *Liquid Crystals, Solid State Physics, Supplement No. 14*, edited by L. Liebert (Academic Press, New York, 1978), p. 147.
[4] R. C. DiPrima and H. L. Swinney, in *Hydrodynamic Instabilities and the Transition to Turbulence*, edited by H. L. Swinney and J. P. Gollub (Springer-Verlag, New York, 1981), p. 139.
[5] M. M. Chen and J. A. Whitehead, J. Fluid Mech. **31**, 1 (1968); F. H. Busse and J. A. Whitehead, J. Fluid Mech. **47**, 305 (1971).
[6] J. R. de Bruyn, C. Bizon, M. D. Shattuck, D. Goldman, J. B. Swift, and H. L. Swinney, Phys. Rev. Lett. **81**, 1421 (1998).
[7] S. Nasuno and S. Kai, Europhys. Lett. **14**, 779 (1991).
[8] J. Plumecoq, C. Szwaj, D. Derozier, M. Lefranc, and S. Bielawski, Phys. Rev. A, **64**, 061801 (2001).
[9] H. Bénard, Rev. Gen. Sci. Pure Appl., **11**, 1261 (1900).
[10] M. Bestehorn, Phys. Rev. E, **48**, 3622 (1993).
[11] Q. Ouyang and H. Swinney, Nature (London) **352**, 610 (1991).
[12] R. Neubecker and E. Benkler, Phys. Rev. E, **65**, 66206 (2002).
[13] B. Caroli, C. Caroli, and B. Roulet, J. Cryst. Growth **68**, 677 (1984).
[14] P. B. Umbanhowar, F. Melo, and H. L. Swinney, Physica (Amsterdam) **249A**, 1 (1998).
[15] B. Echebarria and C. Pérez-Garciá, Europhys. Lett. **43**, 35 (1998).
[16] Y.-N. Young and H. Riecke, Physica (Amsterdam) **163D**, 166 (2002).
[17] J. R. de Bruyn, E. Bodenschatz, S. W. Morris, S. P. Trainoff, Y. Hu, D. S. Cannell, and G. Ahlers, Rev. Sci. Instrum. **67**, 2043 (1996).
[18] T. Tam, D. Ohata, and M. Wu, Phys. Rev. E **61**, 9(R) (2000).
[19] David A. Egolf, Ilarion V. Melnikov, and Eberhard Bodenschatz, Phys. Rev. Lett. **80**, 3228 (1997).
[20] S. Ciliberto, P. Coullet, J. Lega, E. Pampaloni, and C. Pérez-García, Phys. Rev. Lett. **65**, 2370 (1990).
[21] D. Semwogerere and M. F. Schatz, Phys. Rev. Lett. **88**, 054501 (2002).
[22] M. M. Sushchik and L. S. Tsimring, Physica (Amsterdam) **74D**, 90 (1994).